

# The Effect of Percolation on the Capacitance of Supercapacitor Electrodes Prepared from Composites of Manganese Dioxide Nano-Platelets and Carbon Nanotubes

Thomas M. Higgins,<sup>1,2</sup> David McAteer,<sup>1,2</sup> João Carlos Mesquita Coelho,<sup>1,3</sup> Beatriz Mendoza Sanchez,<sup>1,3</sup> Zahra Gholamvand,<sup>1,2</sup> Greg Moriarty,<sup>1,2</sup> Niall McEvoy,<sup>1,3</sup> Nina Christina Berner,<sup>1,3</sup> Georg Stefan Duesberg,<sup>1,3</sup> Valeria Nicolosi<sup>1,2,3</sup> and Jonathan N. Coleman<sup>1,2\*</sup>

<sup>1</sup>*CRANN and AMBER research centres, Trinity College Dublin, Dublin 2, Ireland.*

<sup>2</sup>*School of Physics, Trinity College Dublin, Dublin 2, Ireland.*

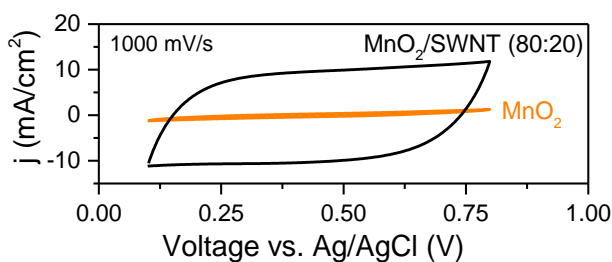
<sup>3</sup>*School of Chemistry, Trinity College Dublin, Dublin 2, Ireland.*

[\\*colemaj@tcd.ie](mailto:*colemaj@tcd.ie)

## ABSTRACT

Here we demonstrate significant improvements in the performance of supercapacitor electrodes based on 2D MnO<sub>2</sub> nano-platelets by the addition of carbon nanotubes. Electrodes based on MnO<sub>2</sub> nano-platelets do not display high areal capacitance because the electrical properties of such films are poor, limiting the transport of charge between redox sites and the external circuit. In addition, the mechanical strength is low, limiting the achievable electrode thickness, even in the presence of binders. By adding carbon nanotubes to the MnO<sub>2</sub>-based electrodes, we have increased the conductivity by up to eight orders of magnitude, in line with percolation theory. The nanotube network facilitates charge transport, resulting in large increases in capacitance, especially at high rates, around 1 V/s. The increase in MnO<sub>2</sub> specific capacitance scaled with nanotube content in a manner fully consistent with percolation theory. Importantly, the mechanical robustness was significantly enhanced, allowing the fabrication of electrodes that were 10 times thicker than could be achieved in MnO<sub>2</sub>-only films. This resulted in composite films with areal capacitances up to 40 times higher than could be achieved with MnO<sub>2</sub>-only electrodes.

**KEYWORDS:** Supercapacitor, percolation, capacitance, nanotube, manganese dioxide, carbon nanotube composite, electrode, thin film



TOC figure

Over the last decade, the study of 2-dimensional (2D) nanomaterials has become one of the most exciting areas of nanoscience. Catalysed by the exciting properties of graphene,<sup>1</sup> a large research field has grown up around the study of 2D materials such as MoS<sub>2</sub>,<sup>2, 3</sup> MnO<sub>2</sub><sup>4</sup> and most recently phosphorene.<sup>5</sup> These materials can either be grown over large areas<sup>2</sup> or produced in large quantities by exfoliation of layered compounds.<sup>6-9</sup> A host of 2D nanostructures have shown great promise for applications in a range of areas from optoelectronics<sup>3</sup> to electrochemistry.<sup>2, 10, 11</sup> Possibly the most exciting area where 2D materials have shown potential is in the generation and storage of energy. The versatility of these materials is clearly illustrated by the range of energy applications where they have been applied: transition metal dichalcogenides such as MoS<sub>2</sub> and WS<sub>2</sub> have been demonstrated as hydrogen evolution catalysts,<sup>2, 12, 13</sup> electrodes in lithium ion batteries<sup>2, 14, 15</sup> and dye-sensitised solar cell electrodes;<sup>16</sup> layered oxides such as TiO<sub>2</sub> and MnO<sub>2</sub> as lithium ion battery electrodes<sup>17-19</sup> or oxygen reduction catalysts;<sup>20</sup> while 2D materials such as Bi<sub>2</sub>Te<sub>3</sub> have been demonstrated as efficient thermoelectrics.<sup>21</sup>

However, one of the most promising applications of 2D materials is as electrodes in supercapacitors. Many of these compounds display redox properties resulting in levels of Faradaic- or pseudo- capacitances much higher than those achievable from electrochemical double layer effects alone.<sup>22-24</sup> Indeed, the theoretical pseudocapacitance of MnO<sub>2</sub> is 1370 F/g, which is extremely high.<sup>25</sup> Moreover, a growing selection of layered oxides and hydroxides are showing great promise in this area.<sup>3, 26-35</sup>

To best employ the high intrinsic pseudocapacitance of any material requires the maximum number of redox active sites be in contact with the electrolyte and therefore available for charge storage. This makes the layered oxides described above extremely attractive so long

as they can be exfoliated into thin flakes. Indeed, electrodes fabricated from monolayers of MnO<sub>2</sub> or RuO<sub>2</sub> would be expected to display very high capacitances as all redox sites would be adjacent to the electrolyte. Probably the best way to achieve this in practise is to employ liquid exfoliation of layered compounds to give large quantities of suspended flakes in a processable form.<sup>4, 7</sup> Even though the flakes produced by such techniques may not be exclusively monolayers, but display a range of thicknesses up to 10 layers thick, the scalability<sup>36</sup> of such exfoliation processes coupled with the intrinsic processability<sup>7</sup> of liquid suspensions makes liquid exfoliation an attractive way to produce supercapacitor electrodes.

However, whether for supercapacitors produced by liquid processing or other means, experimental pseudocapacitances approaching the theoretical values are seldom achieved except for ultra-thin electrodes which are charged and discharged very slowly.<sup>25, 37, 38</sup> It has not proven straightforward to transform such promise into practical supercapacitors with high absolute capacitance. One of the reasons for this is that the specific capacitance (*i.e.* in F/g) generally falls rapidly with electrode thickness. This was noted by Lee *et al.*, reporting a specific capacitance of only 0.13 F/g for a 20 μm thick MnO<sub>2</sub> film (2 mV/s).<sup>39</sup> Such unfavourable thickness-dependence is a general problem for low-conductivity electrode materials and is associated with limitations in the transport of both electrons and ions.<sup>40, 41</sup> These problems are serious as they also mean that the available capacitance falls dramatically at high charge/discharge rates. In addition, the low electrical conductivity results in high equivalent series resistances and consequently low power densities.

One common solution to this problem is to combine the pseudocapacitive material with a nanoconductor such as carbon-black, acetylene black, carbon nanotubes or graphene to form a composite electrode.<sup>30, 39, 42-46</sup> It is worth noting that such an approach is straightforward when using solution processing techniques.<sup>6, 47</sup> Numerous researchers have shown that this strategy can result in increased capacitance by facilitating transport of charge from redox sites to the external circuit.<sup>33, 39, 42, 48, 49</sup> However, there are a number of problems with this approach. Most important is that any addition of nano-conductor reduces the fraction of capacitive material present. Thus, it is critical to fully characterise such composites to identify the minimum nano-conductor mass fraction required. This requires the preparation of a large number of composite electrodes over a wide range of mass fractions and their characterisation *via* complementary electrical and capacitive measurements. Particular care must be taken with novel composites where both phases are nano-materials which may have different dimensionalities (*e.g.* 1D

nanotubes and 2D nanosheets or nano-platelets). The electrical properties<sup>47</sup>, and so the optimum nano-conductor content, will vary strongly across composite types. This means extensive optimisation is required in every case, which is not generally done. These problems are especially relevant for composites containing 2D nano-materials, in particular, those involving new materials are not yet well documented. Indeed, we suggest that for most composite supercapacitor electrodes the interplay between capacitance and charge transport is poorly understood. In our view, the biggest difficulty is the lack of real understanding of the factors influencing the transport of charge from redox site to external circuit *via* the nano-conductor material. Other problems are associated with the composite production technique which is generally cumbersome or costly and not suitable for real commercial devices.<sup>50,51</sup> One manifestation of this is the fact that impressive data associated with very thin electrodes are often presented without the corresponding data for the thick electrodes that are required by industry. This is an issue because, in many cases, severe degradation of performance with increased thickness is to be expected.

In this work we address these problems. Using MnO<sub>2</sub> nano-platelets as a model 2D system, we demonstrate a simple method to produce supercapacitor electrodes based on solution processing. We show that the capacitance of these electrodes falls off with increasing electrode thickness and scan rate as would be expected for a material limited by low electrical conductivity. Equally problematic, the electrodes are not mechanically robust and become unstable beyond thicknesses of 1.7  $\mu\text{m}$ . To resolve these issues we use simple solution-processing techniques to prepare composite electrodes of MnO<sub>2</sub> nano-platelets mixed with carbon nanotubes. We show that the electrical conductivity of such composites can be tuned over eight orders of magnitude and is controlled by percolation theory. Electrochemical testing is used to demonstrate that the addition of even small amounts of nanotubes has a dramatic effect on charge storage properties, with up to  $\times 25$  increase in capacitance observed at scan rates of  $\sim 1000$  mV/s. Importantly, we explore the mechanism, finding the capacitance increase to scale with nanotube volume fraction as predicted by percolation theory. Another practical advantage of this approach is that the composite electrodes were much more mechanically robust, allowing the production of much thicker films giving up to a 40-fold increase in areal capacitance compared to MnO<sub>2</sub> alone.

## RESULTS AND DISCUSSION

### *Single component films of MnO<sub>2</sub> or SWNT*

Layered manganese dioxide was prepared by a modified version<sup>52</sup> of the co-precipitation method described by Jiang *et al.*<sup>45</sup> (see Methods). This procedure results in a brown dispersion containing ~0.2 mg/ml MnO<sub>2</sub> dispersed in isopropanol. TEM analysis (figure 1 A-B) showed the dispersed material to be in the form of thin nano-platelets with mean lateral size of ~200 nm (see SI figure S1). We note that such samples always contain a small population of relatively large crumpled objects such as that in the bottom of figure 1B. Thin films of MnO<sub>2</sub> nano-platelets were produced by vacuum filtration for Raman and XPS analysis. A typical Raman spectrum is shown in figure 1C and displays a dominant feature at ~645 cm<sup>-1</sup>, which we attribute to the symmetric stretching vibration  $\nu_2(\text{Mn-O})$  of MnO<sub>6</sub>, as expected for layered MnO<sub>2</sub>.<sup>53-55</sup> The shoulder observed on the left hand side of this primary peak (~575 cm<sup>-1</sup>) can be attributed to the  $\nu_3(\text{Mn-O})$  stretching vibration associated with MnO<sub>6</sub> octahedra.<sup>56</sup> XPS measurements of the Mn 2p and O 1s core-levels (Figure 1D and E) show the expected MnO<sub>2</sub> components in the correct stoichiometry, with a ratio of manganese to oxygen very close to 50 %. The Mn 2p<sub>3/2</sub> peak has been fitted with five multiplet components in accordance with the parameters established for MnO<sub>2</sub> by Biesinger *et al.*<sup>57</sup> The additional Mn<sup>3+</sup> component can be attributed to X-ray damage and/or other oxide species like Mn<sub>2</sub>O<sub>3</sub>, but only constitutes a very minor part of the spectrum. Apart from the main MnO<sub>2</sub> component, the deconvoluted O 1s peak also shows contributions from the SiO<sub>2</sub> substrate, nitrates which are most likely associated with the Mn(NO<sub>3</sub>)<sub>2</sub> starting material and a minor contribution from adventitious carbonates. This analysis clearly shows the synthesised material to be predominately layered MnO<sub>2</sub>.

Once the nature of the dispersed material was confirmed, we used vacuum filtration to prepare a range of thin films with varying nano-platelet mass per unit area (M/A). The mass was controlled *via* the volume of dispersion filtered while a small quantity (10 wt%) of ethyl cellulose (EC) was added as a binder. The film M/A varied from 2 to 160  $\mu\text{g}/\text{cm}^2$ , a relatively broad range as compared to previous work (Comparison: Pang *et al.*:<sup>37</sup> 1-14  $\mu\text{g}/\text{cm}^2$ , Hu *et al.*:<sup>58</sup> 130-150  $\mu\text{g}/\text{cm}^2$ ). After filtration, pieces of the films (A~0.25 cm<sup>2</sup>) were transferred from the nitrocellulose filter membranes onto ITO-coated glass current collectors, using acetone to dissolve the membrane.<sup>59</sup>

Film thicknesses were determined using profilometry, revealing that the M/A loading range corresponds to thickness varying from 40 nm to 1.7  $\mu\text{m}$  (see SI figure S2). Despite the inclusion of the ethyl cellulose, we found it impossible to prepare electrodes of the MnO<sub>2</sub>

thicker than 1.7  $\mu\text{m}$ , due to poor mechanical properties leading to difficulties in transfer. We measured the film density as 0.95  $\text{g}/\text{cm}^3$  suggesting a high film porosity of  $\sim 80\%$  (using  $\rho_{\text{MnO}_2} = 5 \text{ g}/\text{cm}^3$ ). This morphology is attractive for electrochemical capacitor applications due to the combination of high of surface to bulk atomic ratio and porosity, enabling ready access of electrolyte counter ions to internal surface area of the electrode.

Electrochemical testing was performed to investigate the charge storage properties of the  $\text{MnO}_2$  films. Cyclic voltammetry (CV) was carried out using 0.5 M  $\text{K}_2\text{SO}_4$  electrolyte in a three electrode configuration. Before measurement, each film was conditioned by applying 50 CV cycles between 0.1 and 0.8 V *versus* Ag/AgCl ( $dV/dt=100 \text{ mV/s}$ ) to ensure a stable electrochemical response. Next, CVs were recorded at a variety of scan rates from 10 to 5000  $\text{mV/s}$ . The slowest and fastest scan rates correspond to charging/discharging times of 70 sec and 0.14 sec respectively. These charging/discharging times are suitable for many supercapacitor applications.<sup>60</sup>

The typical CV response of an ultra-thin  $\text{MnO}_2$  electrode ( $t\sim 40 \text{ nm}$ ) at two scan rates (50 and 5000  $\text{mV/s}$ ) is shown in figure 2A. To facilitate comparison we normalised the current response to both scan rate and the mass of active material, yielding a differential gravimetric capacitance. The shape of the CV curves are broad and near-rectangular, typical of the pseudocapacitive response of this material<sup>44</sup> at 50  $\text{mV/s}$ , Faradaic features can be discerned, centered at 0.5 V on oxidation, and 0.4 V on reduction. A slow current rise, even for the thin film electrodes, indicated the presence of resistive character. The capacitance was calculated by integrating the current passed within the potential window (see Methods). We calculated a relatively high specific capacitance (C/M) for this material ( $\sim 200 \text{ F/g}$  at 50  $\text{mV/s}$ ), typical for a thin film of  $\text{MnO}_2$  charged relatively slowly.<sup>58, 61</sup> This value decreases only slightly at very high scan rate ( $\sim 90 \text{ F/g}$  at 5000  $\text{mV/s}$ ).

Characterisation of films with thickness in the nanometer range is useful to evaluate the quality of the material. However, for many applications where greater absolute capacitance is required the electrode thickness needs to be scaled up. Therefore it is important to evaluate how capacitance varies with electrode thickness. To investigate this we have prepared thicker electrodes and evaluated their charge storage behaviour in a similar manner. Figure 2B shows a CV of a 1.7  $\mu\text{m}$  thick  $\text{MnO}_2$  film. We observe that C/M has decreased by a factor of  $\sim 10$  at 50  $\text{mV/s}$  and a factor of  $\sim 100$  at 5000  $\text{mV/s}$ , compared with the 40 nm film. The CV shape

exhibits a more resistor-like behaviour for thicker films, and the Faradaic features observed for the thin films are no longer perceivable, even at low scan rates (Figure S4). We emphasise that even these MnO<sub>2</sub> films are still relatively thin; commercial supercapacitor electrodes based on porous carbon typically have thicknesses of 10-100s of microns.<sup>62</sup>

To demonstrate this behaviour more clearly we have plotted C/M as a function of scan rate for three different electrode thicknesses (Figure 2C) and as a function of thickness for three different scan rates (Figure 2D). In both cases we observe impaired specific capacitance when going to thicker films and faster charge/discharge rates. As described in the introduction, such results are consistent with electrodes which are limited by poor electrical performance.<sup>39, 22, 33, 37, 48, 63-68</sup> In particular, the symmetry between these temporal and spatial dependencies suggests they are determined by the same underlying electrode properties, namely those determining the transport of charge between active sites and the external circuit. Using the four-probe technique, we measured the electrical conductivity of the thin films of MnO<sub>2</sub> nano-platelets used here to be  $\sim 1.7 \times 10^{-5}$  S/m. This low conductivity is similar to values reported by others<sup>40, 41</sup> and would be expected to limit supercapacitor performance. Understanding how these effects can be overcome is crucial for the design of supercapacitor electrodes with high absolute capacitance, particularly at high power.

In contrast, the high electrical conductivity of many carbon-based materials (among other reasons) makes them excellent candidates as high performance supercapacitor electrodes. To compare with the MnO<sub>2</sub> data described above, we have prepared disordered network films of single walled carbon nanotubes (SWNTs) of various thicknesses. We measured the film conductivity to be  $\sim 2 \times 10^5$  S/m, which is in agreement with previous reports.<sup>69</sup> Cyclic voltammetry, carried out under the same conditions as for MnO<sub>2</sub>, showed highly rectangular behaviour (see SI figure S3), indicating close to an ideal capacitive response with a small time constant. The gravimetric capacitance was virtually invariant with both thickness and scan rate at  $\sim 10$  F/g (figure 2E and F), as reported by other authors.<sup>49, 70</sup>

It is clear from this work that thin films of MnO<sub>2</sub> have great potential as supercapacitor electrodes but are limited by the poor conductivity resulting in disappointing performance at high rates and electrode thickness. Indeed, overcoming electronic transport limitations of pseudocapacitive materials in general is key to achieving high performance electrodes. As discussed by a number of authors,<sup>49, 63</sup> a simple solution is to add carbon nanotubes to the MnO<sub>2</sub>

electrode resulting in the formation of a conducting network to facilitate transport of charge from redox sites to the external circuit. Furthermore, this strategy is known to improve mechanical properties of films containing layered materials and may assist with electrolyte accessibility by preventing restacking of adjacent sheets.<sup>27, 71</sup>

### *Composite films of MnO<sub>2</sub> and SWNT*

In order to test the effect of adding carbon nanotubes to films of MnO<sub>2</sub> nano-platelets, we prepared composite films with a range of SWNT/MnO<sub>2</sub> mass ratios. This was achieved by simple mixing of appropriate volumes of the two component dispersions followed by vacuum filtration and film transfer (see Methods). In this study, we chose a fixed loading of MnO<sub>2</sub> (160 µg/cm<sup>2</sup>) to which increasing quantities of SWNTs were added, forming composites with nanotube mass fractions of up to 40 wt% ( $M_f = M_{NT} / (M_{NT} + M_{MnO_2})$ ). This method of composition variation differs somewhat from others<sup>72, 73</sup> where the total film mass is kept constant and the masses of both components are altered simultaneously. By keeping the MnO<sub>2</sub> mass constant for all films, our approach makes analysis of the way MnO<sub>2</sub> pseudocapacitance varies with film composition more straightforward. In doing so, we found that while the film thickness is relatively constant at ~1.5 µm up to M<sub>f</sub>=20 wt%, addition of SNWTs beyond this loading caused the film thickness to increase, reaching ~3 µm for a mass fraction ~40 wt% (see SI figure S5). The fixed MnO<sub>2</sub> M/A of 160 µg/cm<sup>2</sup> was chosen because it corresponds to the greatest thickness at which we could produce mechanically robust MnO<sub>2</sub>-only films for comparison, and is a thickness where the capacitance of MnO<sub>2</sub> is clearly electrically limited (figure 2C-D). Additionally, while remaining relatively thin we minimised the influence of ionic transport which cannot be ignored for very thick electrodes.

SEM images of an MnO<sub>2</sub>-only film and two composite films (M<sub>f</sub>=1 and 25 wt%) are shown in figure 3A-C. Even at 1 wt% loading, the presence of the nanotubes is apparent. The images at higher loadings suggest effective mixing of the two components, with the MnO<sub>2</sub> intimately incorporated within the nanotube network. One very important point is that addition of any amount of SWNTs greatly improved the film's mechanical integrity, making the inclusion of binder (EC) unnecessary. This is not unexpected as we have previously observed films of exfoliated 2D materials to be very brittle, but to become much more robust on addition of nanotubes.<sup>6, 74</sup> This contrasts with previously reported composite electrodes where the conductive additive has not also acted as binder.<sup>44, 75</sup> In addition, the composite films are



extremely porous, containing free volumes of >75 % for all mass fractions (see SI, figure S5). This is advantageous as it should allow free access of the electrolyte to the internal surface of the electrode. On the other hand, a high porosity will ultimately reduce the scope for high volumetric capacitance.

Using the four-probe technique, we measured the in-plane electrical conductivity for MnO<sub>2</sub>/SWNT composites with a range of nanotube contents. The conductivity data is plotted in figure 3D where the nanotube content is represented as the volume fraction,  $\phi$  ( $\phi = V_{NT} / (V_{NT} + V_{MnO_2})$ ). We found that the DC conductivity increases rapidly with addition of small amounts of nanotubes, reaching ~100 S/m for  $\phi=1$  vol% and approaching 10<sup>5</sup> S/m for  $\phi=25$  vol%. This behaviour is qualitatively similar to that observed previously for composites of MoS<sub>2</sub> nano-platelets mixed with carbon nanotubes.<sup>6, 47</sup> The electrical properties of such insulator/nanoconductor composites is described by percolation theory.<sup>76</sup> In this framework the film conductivity is expected to be very low until a critical volume fraction of nanoconductors is reached, the electrical percolation threshold,  $\phi_{c,e}$ . Above the percolation threshold, the conductivity is described by<sup>76</sup>

$$\sigma = \sigma_0 (\phi - \phi_{c,e})^n \quad (1)$$

where  $\sigma_0$  is related to the conductivity of the nanoconductor and  $n$  is the percolation exponent.<sup>77</sup> Fitting our data gives a very low electrical percolation threshold of  $\phi_{c,e}=0.16$  vol%,  $\sigma_0$  of 1.4×10<sup>6</sup> S/m and a percolation exponent of 1.82. We note that the percolation threshold for composites with 1D fillers is thought to scale with the diameter to length ratio of the filler particles.<sup>78</sup> Thus, very low percolation thresholds such as that found here are often observed for composites based on carbon nanotubes<sup>77</sup>. This is a significant advantage for our purpose, as a small percolation threshold means significant conductivities can be achieved at relatively low  $\phi$ , meaning very little capacitive material has to be sacrificed to introduce the conductive paths.

### *Composite Supercapacitor Electrodes*

If relatively thick MnO<sub>2</sub>-only electrodes display capacitances which are limited by the electrical conductivity of MnO<sub>2</sub>, the data in figure 3D would lead us to expect the addition of nanotubes to result in significant capacitance enhancements. To test this, we measured CVs for a range of composites as well as single component films. In all cases, the MnO<sub>2</sub> mass was kept

constant at  $160 \mu\text{g}/\text{cm}^2$  resulting in film thicknesses in the range  $1.5\text{-}3 \mu\text{m}$  (SI figure S5). Shown in figure 4A are the current responses of three composite films to linear potential sweeps with  $dV/dt=1000 \text{ mV/s}$ . The first thing to note is a considerable increase in current density as nanotube content is increased. This strongly supports the idea that the introduction of conductive paths facilitates the accessibility of redox sites. However, the shape of the CV curves is also of interest. The response of a simple series resistor-capacitor model is given by

$$j = \frac{C}{A} \frac{dV}{dt} (1 - e^{-t/\tau}) \quad (2)$$

where  $j$  is the current density,  $A$  is the device area and  $\tau = R_{ESR} C$  ( $R_{ESR}$  is the equivalent series resistance which is closely related to the electrode resistance<sup>79</sup>). It is clear that increasing the SWNT content results in reduced  $\tau$ , suggesting a substantial reduction of  $R_{ESR}$  due to the presence of the nanotubes. This effect is also evident, though less pronounced, at slow scan rates (figure S4) and even with 33 wt% nanotubes, the subtle Faradiac features of the  $\text{MnO}_2$ -only films can be discerned. Similar observations regarding CV shape were made by Lee *et al.*<sup>39</sup> and Kim *et al.*<sup>48</sup> on adding carbon black to  $\text{MnO}_2$ .

We can quantify this capacitance increase by plotting the measured capacitance of the composite film,  $C_T$ , normalised to total film mass,  $M_T$ , measured at three scan rates, as a function of nanotube mass fraction in figure 4B (N.B.  $M_T = M_{\text{MnO}_2} + M_{\text{NT}}$  and assuming both  $\text{MnO}_2$  and NTs contribute to the capacitance,  $C_T = C_{\text{MnO}_2} + C_{\text{NT}}$ ). It is clear that, for all scan rates, the capacitance increases dramatically upon addition of even a few percent of nanotubes before falling off at high mass fraction. The SWNT loading providing maximum capacitance falls in the range of 5-15 wt%, shifting slightly to higher loadings with increasing scan rate. In some cases, the improvements are impressive: for the 500 mV/s data a  $\times 15$  increase in  $C_T/M_T$  was observed at  $M_T=11 \text{ wt\%}$  compared to the  $\text{MnO}_2$ -only electrode. Beyond the optimised values, the specific capacitance decreases as the relative nanotube content in the films increases, approaching the nanotube-only value of  $\sim 10 \text{ F/g}$  (a value which was invariant with scan rate over the range studied in this work. Overall, this behaviour is not what would be expected from the rule of mixtures (dashed lines), as would apply if both  $\text{MnO}_2$  and SWNTs were contributing to the capacitance only as per their individual specific capacitances.

The peaked behaviour observed in figure 4B has been observed before in supercapacitors formed from mixtures of activated carbon/carbon black<sup>80</sup> and carbon aerogels

filled with nanoconductors such as carbon black, nanotubes and carbon fibres.<sup>81</sup> In both of these publications, it was suggested that the peak capacitance occurred at the percolation threshold. However, comparing the results in figure 3D and figure 4B shows the peak capacitance to occur at volume fractions substantially above the electrical percolation threshold. This optimum loading of carbon nanotubes (5-15 wt%) is relatively low compared to the literature where (often unoptimised and therefore poorly justified) conductor contents tend to fall in the range 15-25 %.<sup>39, 44, 48, 49, 70, 82-85</sup>. Obviously lower conductor contents are desirable from an economic standpoint given the present relative cost of these two materials.

That the capacitance data in figure 4B does not follow the rule of mixtures suggests the increase in capacitance is due to the addition of conducting paths to the MnO<sub>2</sub> electrode. The presence of these paths seemingly “activates” the nearby MnO<sub>2</sub> by enabling the transport of stored charge to and from the current collector. To examine this suggestion, we should consider the effect of nanotube content on the specific capacitance due only to the MnO<sub>2</sub>. To do this, we subtract off the contribution to the capacitance associated with the nanotubes (*i.e.* estimated using  $C_{NT} / M_{NT}$  of 10 F/g) and normalise to the mass of MnO<sub>2</sub> (*i.e.* we calculate  $(C_T - C_{NT}) / M_{MnO_2}$ ). This data is shown in figure 4C plotted *versus* scan rate for composite electrodes with a number of nanotube contents. Shown for comparison is the equivalent data for an MnO<sub>2</sub>-only film of equivalent M/A. This data shows the presence of nanotubes to considerably increase the capacitance associated with the MnO<sub>2</sub> at all scan rates. However, the effect is particularly apparent at high scan rates with the MnO<sub>2</sub> capacitance increasing from ~2 F/g in the MnO<sub>2</sub>-only film to ~42 F/g for the film with 33 wt% SWNT (dV/dt=1000 mV/s). That these increases are due to conductivity enhancement rather than morphological effects in response to the addition of nanotubes can be seen by measuring the film porosity as a function of nanotube content (see SI fig S5B). This data clearly shows the porosity to be invariant with nanotube content ruling out the possibility that the nanotubes somehow open the network, allowing easier access of ions to the internal surface.

In practical terms, what is important is the increase in specific electrode capacitance which can be achieved by adding nanotubes. To show this, we plot the ratio of the specific capacitance of a composite electrode to that for an MnO<sub>2</sub>-only electrode (*i.e.*  $(C_T / M_T) / (C / M)_{MnO_2\text{-only}}$ ) *versus* scan rate in figure 4D for a number of mass fractions. While a ×2 increase is found at low scan rates, much larger increases are found at higher scan

rates. The relative capacitance increase peaks at scan rates of ~600-2000 mV/s with a  $\times 20$  increase observed at 2000 mV/s for the 33 wt% sample.

### *Percolation of capacitance in composite films*

To allow future optimisation of solution-processed nanostructured supercapacitor electrodes, it will be necessary to understand the nature of these capacitance increases. The increase in MnO<sub>2</sub> capacitance compared to an MnO<sub>2</sub>-only electrode, normalised by MnO<sub>2</sub> mass, is given by

$$(\Delta C / M)_{MnO_2} = \frac{C_T - C_{NT} - C_{MnO_2\text{-only}}}{M_{MnO_2}} \quad (3)$$

We note that calculation of this parameter is facilitated by the fact that all films have identical MnO<sub>2</sub> mass as described above and in Methods. Shown in figure 5A is  $(\Delta C / M)_{MnO_2}$  plotted *versus* nanotube volume fraction,  $\phi$ , for data collected at two representative scan rates. As illustrated by these plots, data collected at all scan rates display the same features: at low  $\phi$ ,  $(\Delta C / M)_{MnO_2}$  increases non-linearly with  $\phi$  up to  $\phi = \phi_{sat}$ , after which it reaches a constant value which we denote  $(\Delta C / M)_{sat}$ . We will first discuss the low  $\phi$  behaviour before turning to the saturation regime.

As discussed above, it is likely that the observed increases in capacitance are associated with the introduction of conducting paths to the electrode. The conductivity of the overall network is controlled by percolation theory (figure 3D). However, it has previously been shown that, for supercapacitor electrodes based on percolating nanotube networks, the resulting capacitance is also described by percolation theory.<sup>79</sup> This occurs because the capacitance is directly proportional to the number of nanotubes connected to the network, a parameter which is controlled by percolation theory.<sup>76, 79</sup> It is likely that similar phenomena are present in the MnO<sub>2</sub>/SWNT composites under study here. We propose that, as the nanotube volume fraction increases and the network becomes more extensive, the volume of MnO<sub>2</sub> within close proximity of the network increases. This proximate MnO<sub>2</sub> can easily transfer charge to the current collector *via* the nanotube network and so becomes “activated”. Thus, we expect the capacitance to scale with network size and propose that the capacitance increase to be described by a percolative scaling law of the form:

$$(\Delta C / M)_{MnO_2} = (\Delta C / M)_0 (\phi - \phi_{c,c})^{n_c} \quad (4)$$

where  $(\Delta C / M)_0$  is a constant,  $\phi_{c,c}$  is the capacitive percolation threshold and  $n_c$  is the capacitive percolation exponent. We note that, in general, the  $(\Delta C / M)_{MnO_2}$  versus  $\phi$  data is quite scattered, making it difficult to accurately fit a three-unknown function such as equation 4 to the data. To address this, we fixed  $\phi_{c,c}$  at a constant value for all scan rates. Initial trials found that setting  $\phi_{c,c} = \phi_{c,e} = 0.0016$  gave reasonable fits for all scan rates. However, it was found that using  $\phi_{c,c} = 0.003$  gave clearly better fits, especially at low  $\phi$  (15 out of 19 scan rates displayed  $R^2 > 0.9$ ). This can be seen by plotting  $(\Delta C / M)_{MnO_2}$  versus  $\phi - \phi_c$  as shown in figure 5B. This justifies our proposal to use equation 4 and suggests the capacitance is indeed described by percolation theory.

The fact that  $\phi_{c,c} > \phi_{c,e}$  is perhaps not unexpected. The electrical measurements were associated with current flowing in the plane of the composite. However, in the capacitance measurements the composite electrode sits on top of an ITO current collector, with the electrolyte in contact with the top composite surface. In this case, current flow from ITO to redox sites is, on average, out of plane. In thin film composites, we expect the nanotubes to be randomly arranged in the plane of the film but partially aligned with the film surface making in-plane and out-of-plane charge transport non-equivalent. In fact, it has been shown that the percolation threshold for aligned rods is higher than that for randomly arranged rods<sup>86</sup> making the difference between  $\phi_{c,c}$  and  $\phi_{c,e}$  unsurprising.

Fitting gave  $(\Delta C / M)_0$  and  $n_c$  with reasonably low uncertainties for a range of scan rates between 10 and 5000 mV/s. These data are shown in figure 5C-D. The capacitive percolation exponent increases monotonically with scan rate from  $n_c \sim 0.2$  for  $dV/dt = 10$  mV/s to  $n_c \sim 3$  for  $dV/dt = 5000$  mV/s. This is somewhat unexpected as for electrical percolation, the percolation exponent tends to be a property of the network, scaling with parameters such as network uniformity<sup>87</sup> or width of the junction resistance distribution.<sup>88</sup> Such network properties would not be expected to vary with scan rate. The scan rate dependence of  $(\Delta C / M)_0$  is also poorly understood. It follows a similar form as the  $n_c$  versus rate data, increasing continuously with rate. By analogy with electrical percolation<sup>78</sup> we would expect  $(\Delta C / M)_0$  to reflect the material properties of the system. As with the capacitive percolation exponent, we would not expect such a material property to vary with scan rate. However, we suggest that to some

extent these variations in the fit parameters with scan rate may reflect an influence of ionic diffusion constraints, which become important at higher rates. Thorough examination of these effects will require knowledge of how ionic diffusion properties within the electrode vary with nanotube loading in these composites, which is an important question for future work. However, what is not in doubt is that the relative capacitance increase associated with MnO<sub>2</sub> is consistent with percolation theory.

It is probably easier to understand the saturated behaviour. As  $\phi$  is increased, the network becomes more extensive, bringing more and more MnO<sub>2</sub> within proximity of nanotubes. However, at some critical volume fraction,  $\phi_{sat}$ , all MnO<sub>2</sub> in the electrode will be close enough to a nanotube to effectively exchange charge with the network. After this, the capacitance cannot be increased by increasing the volume fraction and it saturates at a value of  $(\Delta C / M)_{sat}$ . The saturation volume fraction,  $\phi_{sat}$ , is plotted *versus* scan rate in figure 5E and clearly is constant at ~6 vol%. This invariance implies that the maximum distance ( $R$ ) over which MnO<sub>2</sub> can exchange charge with the network is scan rate independent. This maximum range defines a shell, of thickness  $R$ , which surrounds the nanotube network and defines the volume of activated MnO<sub>2</sub> *i.e.* the MnO<sub>2</sub> which can effectively transfer charge to the nanotube network. The saturation volume fraction is then the lowest volume fraction where the shell encloses all the MnO<sub>2</sub> in the electrode. Considering a local section of shell, associated with a straight section of nanotube (radius  $r$ ), both of which we model as cylinders, the saturation volume fraction is approximately the nanotube volume divided by the volume enclosed by the shell:  $\phi_{sat} = r^2 / (r + R)^2$ . Taking  $\phi_{sat}=6$  vol% gives  $R \approx 3r$ . Assuming that the nanotubes are in the form of bundles of diameter ~20 nm (as observed previously<sup>69</sup>), means that  $r \sim 10$  nm, giving  $R \sim 30$  nm.

The dependence of  $(\Delta C / M)_{sat}$  on scan rate is shown in figure 5F. Interestingly,  $(\Delta C / M)_{sat}$  increases at low scan rate before reaching a maximum at ~200 mV/s. We note that the position of this maximum is controlled by the details of the rate dependence of both  $n_c$  and  $(\Delta C / M)_0$ . However, it is the presence of this maximum that results in the shape of the curves given in figure 4D.

This work clearly demonstrates the importance of percolation in composite supercapacitors. While a number of papers have suggested percolation to play a role in the

operation of composite supercapacitors,<sup>80, 81, 89</sup> even indicating the onset of capacitance at the electrical percolation threshold,<sup>30</sup> percolation scaling of capacitance has not been observed. We note that Pico *et al.*, when studying nanotube/activated carbon composite, observed rule of mixtures rather than percolative behaviour.<sup>89</sup> However, it is likely that this is due to the relatively high conductivity of the capacitive phase and the moderate difference in conductivities between the components of the composite ( $\times 1000$  compared with  $> \times 10^8$  here). We believe the current study is the first demonstration of percolation of capacitance in composite supercapacitor electrodes (although percolation scaling of capacitance has been observed in single-component nanotube networks).<sup>79</sup> Understanding the nature of such percolation will be critical for the optimisation of capacitive composites.

### *Thick composite films*

As described in the introduction, working supercapacitors must display large areal capacitances,  $C/A$ , to maximise their energy storage capacity. Because  $C/A = \rho t C_T / M_T$ , where  $\rho$  and  $t$  are electrode density and thickness respectively, maximisation of areal capacitance requires  $C_T / M_T$  to remain high even as the film thickness is maximised. However, as described above, electrodes of MnO<sub>2</sub> nano-platelets display two significant problems. Firstly, like all resistive electrode materials  $C_T / M_T$  tends to fall with increasing thickness. Secondly, and equally serious is the problem of poor mechanical integrity of MnO<sub>2</sub> electrodes. As described above, we found it impossible to prepare MnO<sub>2</sub>-only electrodes with  $t > 1.7 \mu\text{m}$  due to severe brittleness. We expect both of these problems to be addressed by the production of MnO<sub>2</sub>-nanotube composites. To test this, we produced a set of composite electrodes ( $\phi = 15 \text{ vol\%}$ , well in the saturated regime) with thicknesses between 1.6 and 17  $\mu\text{m}$ . In all cases the electrodes were mechanically robust with no problems associated with brittleness.

We performed CV measurements to measure the capacitance of these electrodes for a number of scan rates. Shown in figure 6A is the specific capacitance,  $C_T / M_T$ , measured at two scan rates, plotted as a function of thickness (solid symbols). For comparison, the equivalent data is also shown for MnO<sub>2</sub>-only electrodes (open symbols). While the MnO<sub>2</sub>-only capacitance tends to fall off with increasing thickness, it is clear that the composites have higher capacitance for a given thickness compared to the MnO<sub>2</sub>-only. In addition, for the 100 mV/s data, the measured values of  $C_T / M_T$  remain roughly constant as thickness is increased. For the

1000 mV/s data,  $C_T/M_T$  falls with increasing thickness, probably because at this high rate the capacitance becomes diffusion limited. However, even at 1000 mV/s, the capacitance is much higher in the composite than would be achieved for thicker  $MnO_2$ -only films *if they could be made*.

Probably more useful is to plot the data as  $C_T/A$  as we have done in figure 6B. Here, the  $MnO_2$ -only data increases sub-linearly (linearity indicated by dashed line) with  $t$ . However, for the composite, the 100 mV/s data increases linearly, reaching 52 mF/cm<sup>2</sup> at  $t=10.3 \mu m$ . In addition, even though the 1000 mV/s composite data increases sub-linearly, the best composite still displays 11.4 mF/cm<sup>2</sup>, considerably larger than the best  $MnO_2$  film. Similar values were obtained by Okamura *et al.*<sup>90</sup> who prepared Mn/Mo mixed oxide composite electrodes with carbon nanotubes, measuring 20.4 mF/cm<sup>2</sup> for a 4.1  $\mu m$  film (100 mV/s in 0.5 M  $Na_2SO_4$  electrolyte) and Wen *et al.*<sup>91</sup> who prepared  $MnO_2$  composites with carbon black, measuring 20 mF/cm<sup>2</sup> for a 20  $\mu m$  film (10 mV/s, 0.1 M KCl).

In figure 6C, we compare the areal capacitance for the thickest  $MnO_2$ -only film ( $t=1.7 \mu m$ ) with that of the best performing composite film ( $t=10.3 \mu m$ ). It is clear that the composite massively outperforms the  $MnO_2$ -only film at all scan rates. We can quantify the improvement shown in figure 6C by plotting the ratio of composite to  $MnO_2$ -only capacitances *versus* scan rate in figure 6D. This graph shows a better than tenfold improvement in areal capacitance at all scan rates below  $\sim 3000$  mV/s. Indeed at scan rates close to 500 mV/s, enhancements of  $\times 40$  are achieved. We note that these improvements are due to the combination of improved  $MnO_2$  capacitance due to improved electrical transport and the ability to prepare thicker electrodes due to the presence of nanotubes.

## CONCLUSIONS

We have demonstrated that supercapacitor electrodes can be easily fabricated by solution processing methods from  $MnO_2$  nano-platelets and  $MnO_2$ -nanotube composites. The  $MnO_2$ -only electrodes displayed capacitances which fell off rapidly with increasing charge/discharge rate and electrode thickness. This is consistent with observations by other authors and is due to the poor electrical conductivity of the  $MnO_2$ . However, on addition of nanotubes, we found the electrode conductivity to increase by eight orders of magnitude in a manner described by percolation theory. Because of the increased conductivity, we observed large increases in capacitance, especially at high rates where a  $>10$ -fold increase in specific



capacitance was observed. This capacitance increase is due to the nanotube network facilitating charge transport from redox sites to the external circuit. We found that the increase in specific capacitance associated with MnO<sub>2</sub> alone increased with nanotube volume fraction as described by percolation theory. However, the percolation fit parameters varied with scan rate in a manner that is currently not understood. At high nanotube content, the specific capacitance associated with MnO<sub>2</sub> alone saturated. The saturation volume fraction was ~6 vol%, a value we associate with the nanotube network activating the entire MnO<sub>2</sub> volume. We test the applicability of these results by preparing thick binder-free MnO<sub>2</sub>-nanotube composites. We find the areal capacitance to be up to 40 times higher than the best MnO<sub>2</sub>-only electrode we could prepare.

To translate the excellent intrinsic charge storage properties of 2D materials into real applications requires they be processed into films and other macroscopic structures. However, for these to be useful the problem of poor electrical conductivity must also be addressed. Here we show that when adding a chosen nanoconductor to form composite films, percolation theory applies not only to the way electrical properties vary with composition but also the extent to which interfacial processes can occur throughout the film as a result of the created electrical pathways. We believe these insights pertain not only to the design of nanostructured supercapacitor electrodes, but to any electrochemical application requiring charge transport between interfacial sites and the external circuit through a nanostructured network current collector.

## METHODS

### *Preparation of MnO<sub>2</sub> dispersions*

Manganese dioxide powder was prepared as described by Jiang *et al.*<sup>45</sup> In brief, 1.7 g of Mn(NO<sub>3</sub>)<sub>2</sub> and 0.5 g of poly(ethylene glycol)-poly(propylene glycol)-poly(ethylene glycol) triblock copolymer (P123) were dissolved into 100 mL of distilled water. The solution was heated to 45 °C and 100 mL of 0.1 M KMnO<sub>4</sub>(aq) was added drop wise under vigorous stirring. The obtained precipitate was filtered under pressure, washed with distilled water and allowed to dry for 24 hours. Chemicals were supplied by Sigma Aldrich, 99.99 % purity.

The resulting MnO<sub>2</sub> powder was then exfoliated by bath sonication to form a stable dispersion in isopropanol (MnO<sub>2</sub> starting concentration, 10 mg/mL). Sonication was carried out for 3 hours using a FisherBrand 11207 sonic bath (37 kHz, 200 W). The dispersion was

then centrifuged for 30 min at 1500 rpm using a Heraeus Multifuge X1 Centrifuge to remove any unstable material.

A stock solution of ethyl cellulose (EC, Sigma Aldrich) was prepared by dissolving this polymer in isopropanol (IPA) while heating at 75 °C (EC concentration, 5 mg/mL). This solution was then added to the stock MnO<sub>2</sub> solution, such that the EC binder:MnO<sub>2</sub> ratio was 1:10. Ethyl cellulose was used as a binder for neat MnO<sub>2</sub> films to improve mechanical integrity.

#### *Preparation of carbon nanotube dispersions*

A stock solution of sodium dodecyl sulfate (SDS, Sigma Aldrich) was prepared by adding this surfactant to Millipore water to an SDS concentration of 5 mg/mL. This solution was then added to arc-discharge single-walled carbon nanotube powder (SWNTs, Iljin Nanotech Co.) such that the surfactant:SWNT mass ratio in the resultant dispersions was 5:1 (SWNT concentration, 1 mg/mL). Each dispersion received 5 minutes of high power tip sonication (VibraCell CVX; 750W, 20 % 60 kHz), was then placed in a sonic bath (Branson 1510-MT sonic bath, 20 kHz) for 1 hour, followed by another 5 minutes of tip sonication. The dispersions were then centrifuged at 5500 rpm for 90 minutes. The supernatant of each dispersion was carefully decanted and combined for further use. We obtained the concentration after centrifugation by measuring the absorbance spectrum (Varian Cary 6000i spectrophotometer) and recording the absorbance per unit length, *A/l*. Using the Lambert – Beer law, the final concentration was calculated using the known extinction coefficient of the SWNT (3389 mL/mg/m at 660 nm).

#### *Film Preparation*

MnO<sub>2</sub> and SWNT only films, and composites of both these materials were prepared by first diluting the stock MnO<sub>2</sub>/EC dispersion tenfold with Millipore water and then combining it with the required amount of the stock SWNT dispersion. All films were prepared by vacuum filtration of the diluted dispersion using porous mixed cellulose ester filter membranes (MF-Millipore membrane, hydrophilic, 0.025 µm pore size, 47 mm diameter). The resulting films (diameter, 36 mm) were cut to the desired dimensions and transferred to polyethylene terephthalate (PET), indium tin oxide (ITO), and Au-coated silicon substrates for electrical conductivity testing, electrochemical testing, and SEM imaging, respectively. The cellulose filter membrane was removed by treatment with acetone vapour and subsequent acetone liquid baths.

## *Film Characterisation*

Film thickness was measured by profilometry using a Dektak 6M, Veeco Instruments. Step profiles were obtained at three locations on the film and averaged. Electrical conductivity values were calculated from resistivity measurements made using a four-point probe technique with a Keithley 2400 source meter (Keithley Instruments, Inc.) and LabView interface (National Instruments, Inc.). Agar Scientific supplied silver paint electrodes were attached to the films and the film width (~4 mm) and electrode separations (~10 mm) were carefully recorded. SEM was performed using a ZEISS Ultra Plus (Carl Zeiss Group). During imaging the accelerating voltage was 5 kV, with a 30  $\mu\text{m}$  aperture and a working distance of approximately 5 mm.

X-Ray photoelectron spectroscopy was performed under ultra-high vacuum conditions (<5.10-10 mbar), using monochromated Al K $\alpha$  X-rays (1486.6 eV) from an Omicron XM1000 MkII X-ray source and an Omicron EA125 energy analyser. An Omicron CN10 electron flood gun was used for charge compensation and the binding energy scale was referenced to the C 1s core-level of the adventitious carbon at 285 eV. The O 1s and Mn 2p core-levels were recorded at an analyser pass energy of 20 eV and with slit widths of 6 mm (entry) and 3 mm x 10 mm (exit). After subtraction of a Shirley background, the spectra were fitted with Gaussian-Lorentzian line shapes.

Raman analysis was performed using a Witec Alpha 300 R with a 532 nm excitation wavelength and an 1800 lines/mm grating. Average spectra were obtained for each sample from line scans consisting of 50 discrete spectra, each with an integration time of 5 min, taken over a line 200  $\mu\text{m}$  in length. A laser power of 400  $\mu\text{W}$ , as measured using a LaserCheck power meter, was employed to minimise sample damage.

Electrochemical properties of the films were examined using cyclic voltammetry in a three electrode electrochemical cell. The cell consisted of a Ag/AgCl reference electrode and an amorphous carbon counter electrode with 0.5 M K<sub>2</sub>SO<sub>4</sub> electrolyte. Electrodes were first cycled at 100 mV/s for 50 cycles between 0.1 and 0.8 V to ensure stable charge/discharge behaviour, followed by 20 cycles each at various scan rates from 10-5000 mV/s (corresponding to charge/discharge times from 0.14 to 70 seconds). Film capacitance was estimated from the cyclic voltammograms by integrating the current passed during the positive and negative potential sweeps:

$$\frac{C}{M} = \frac{1}{(M/A)\Delta V(dV/dt)} \int_v^{v+\Delta v} j dV$$

where  $M/A$  = mass per unit area,  $j$  = areal current density,  $\Delta V$  = potential window (0.7 V),  $dV/dt$  = scan rate. This calculation provides the gravimetric capacitance over the entire potential window and we average the positive and negative portions of the curve. Film area was typically  $0.25 \text{ cm}^2$ .

Acknowledgements: We thank Science Foundation Ireland (11/PI/1087) and the European Research Council (SEMANTICS) for financial support. We acknowledge the CRANN Advanced Microscopy Lab for technical support.

Supporting Information Available: Flake size histogram for  $\text{MnO}_2$ , film thickness as function of loading for  $\text{MnO}_2$  films. CVs for a SWNT only electrode. CVs for  $\text{MnO}_2$  and selected composites at 50 mV/s. Thickness and porosity as a function of loading for composite films. This material is available free of charge *via* the Internet at <http://pubs.acs.org>

## FIGURES

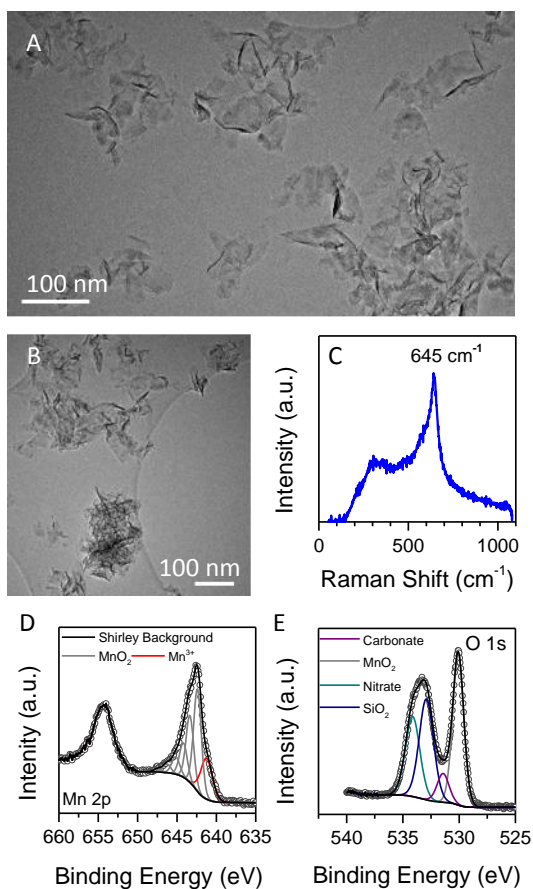


Figure 1: Characterisation of MnO<sub>2</sub> nano-platelets. A-B) TEM images of MnO<sub>2</sub> nano-platelets. C) Raman spectrum measured on vacuum-filtered thin film of MnO<sub>2</sub> nano-platelets. D-E) XPS spectrum measured on vacuum filtered thin film of MnO<sub>2</sub> nano-platelets showing D) Mn 2p peaks and E) O 1s peaks.

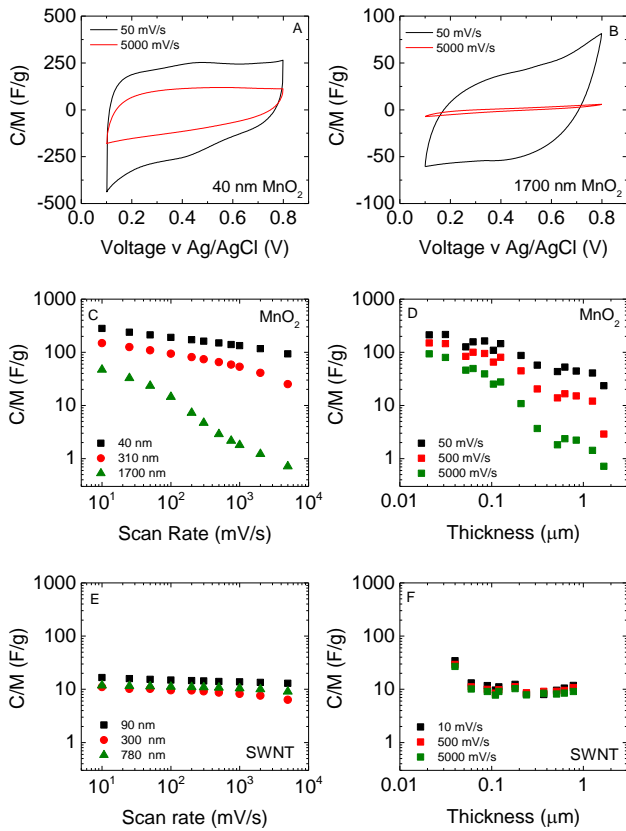


Figure 2: Characterisation of MnO<sub>2</sub> thin film supercapacitor electrodes. A-B) Cyclic voltammograms, measured at two scan rates for electrodes prepared from MnO<sub>2</sub> films with thickness of A) 40 nm and B) 1700 nm. C) Specific capacitance for MnO<sub>2</sub> films of three different thicknesses plotted *versus* scan rate. D) Specific capacitance of MnO<sub>2</sub> films measured at three different scan rates, plotted *versus* film thickness. E) Specific capacitance SWNT films for three different thicknesses plotted *versus* scan rate. F) Specific capacitance of SWNT films measured at three different scan rates plotted *versus* film thickness.

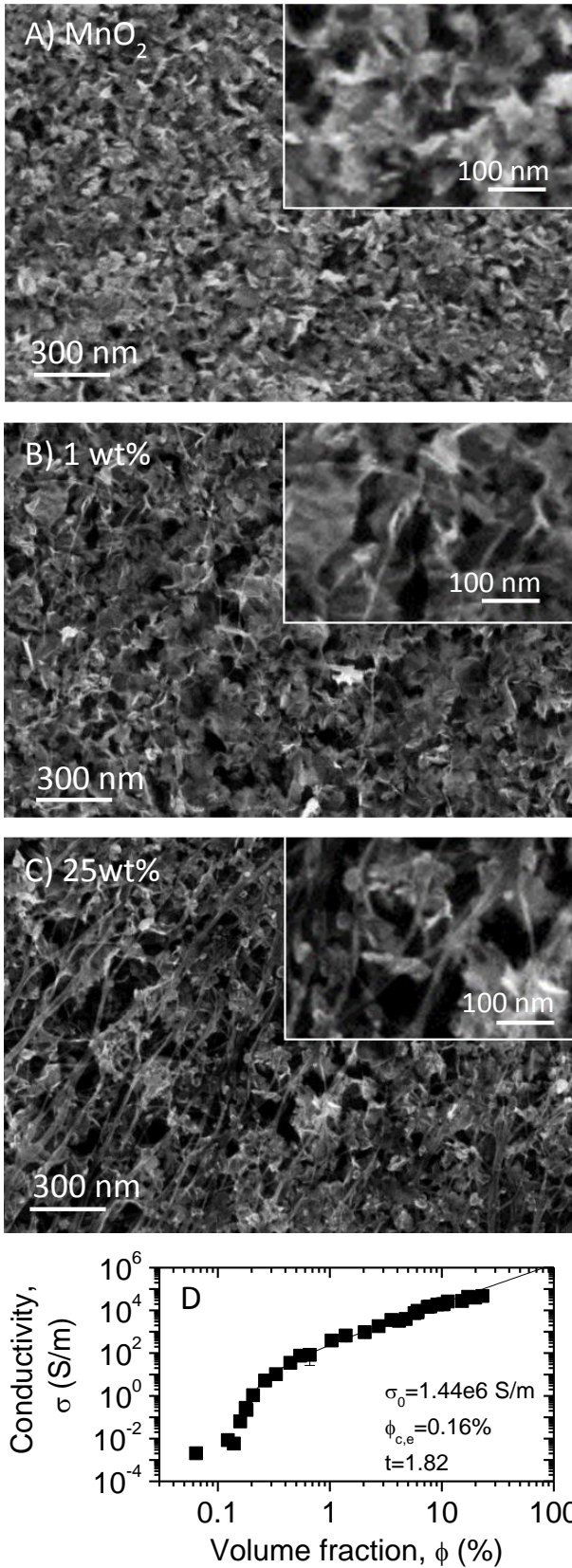


Figure 3: SWNT/MnO<sub>2</sub> composite thin films. A-C) SEM images of A) a thin (~100 nm) MnO<sub>2</sub> film, B) a composite film with 1 wt% SWNTs and C) a composite film with 25 wt% SWNTs. In A-C), the insets show magnified regions. D) In plane electrical conductivity of thin films

plotted *versus* SWNT volume fraction. The line is a fit to percolation theory (equation 1) with the fit constants given in the panel. In all cases the films in D were 1.5-3  $\mu\text{m}$  thick.

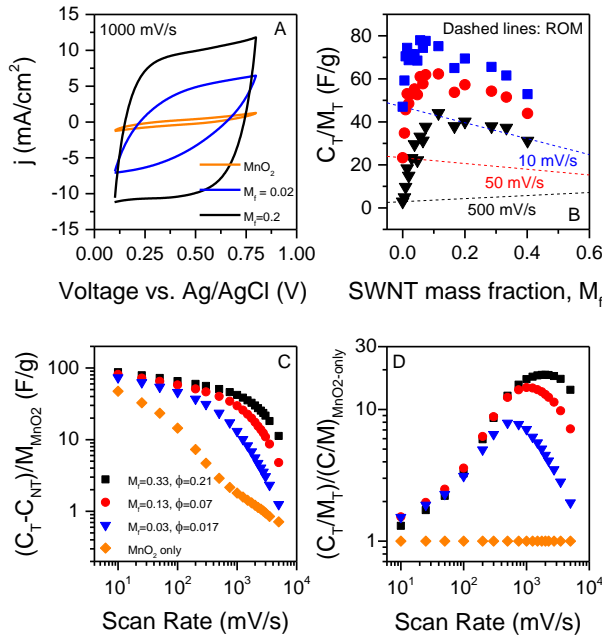


Figure 4: Initial characterisation of MnO<sub>2</sub>/SWNT composite thin films as supercapacitor electrodes. A) Cyclic voltammograms for electrodes prepared from MnO<sub>2</sub> and MnO<sub>2</sub>/SWNT composites with SWNT mass fractions of 2 and 20 wt%. B) Measured total capacitance,  $C_T$ , divided by total electrode mass,  $M_T$ , measured for composite electrodes plotted *versus* SWNT mass fraction,  $M_f$ , for three scan rates, 10, 50 and 500 mV/s. The dashed lines represent the specific capacitance calculated from the Rule of Mixtures (ROM) as would be expected if MnO<sub>2</sub> and SWNT were contributing to the capacitance with no additional effects occurring. C) Specific capacitance associated only with MnO<sub>2</sub> (*i.e.* with SWNT contribution removed) measured for composite electrodes plotted *versus* scan rates for a number of SWNT mass fractions. In the caption, the SWNT volume fraction,  $\phi$ , is also given. D) Increase in specific capacitance due to the presence of SWNTs relative to MnO<sub>2</sub>-only electrodes plotted *versus* scan rate for a number of SWNT mass fractions (see panel C for key). In all cases the films in D were 1.5-2  $\mu\text{m}$  thick.



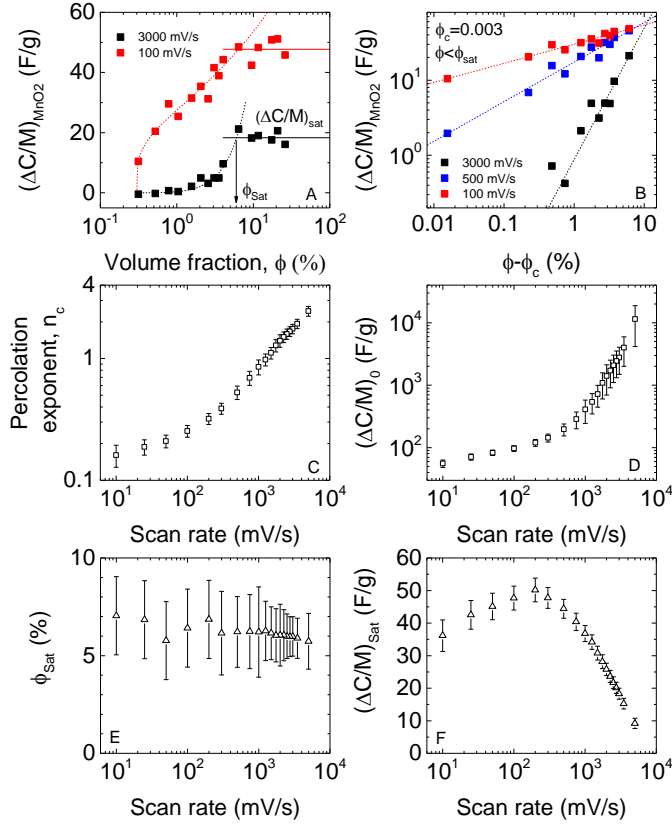


Figure 5: Percolation analysis of thin film supercapacitor electrodes. A) Increase in specific capacitance of MnO<sub>2</sub> due to percolative effect  $(\Delta C/M)_{MnO_2} = (C_T - C_{NT} - C_{MnO_2\text{-only}})/M_{MnO_2}$  (i.e. with SWNT contribution and capacitance of equivalent MnO<sub>2</sub>-only film subtracted off), measured at two different scan rates, plotted *versus* SWNT volume fraction. In all cases the capacitance saturated at a value of  $(\Delta C/M)_{Sat}$  (solid line) for volume fractions above a critical value,  $\phi_{sat}$ . The dashed lines are fits to percolation theory (equation 3). B) Percolation scaling graphs for specific capacitance increase. In all cases the percolation threshold was  $\phi_c=0.3$  vol%. The lines represent fits to percolation theory (equation 3). Only data with  $\phi < \phi_{sat}$  is shown. C- D) Percolation fit parameters plotted *versus* scan rate: the percolation exponent (C) and  $(\Delta C/M)_0$  (D). E-F) Saturated volume fraction,  $\phi_{sat}$ , (E) and saturation capacitance,  $(\Delta C/M)_{Sat}$ , (F) both plotted *versus* scan rate.

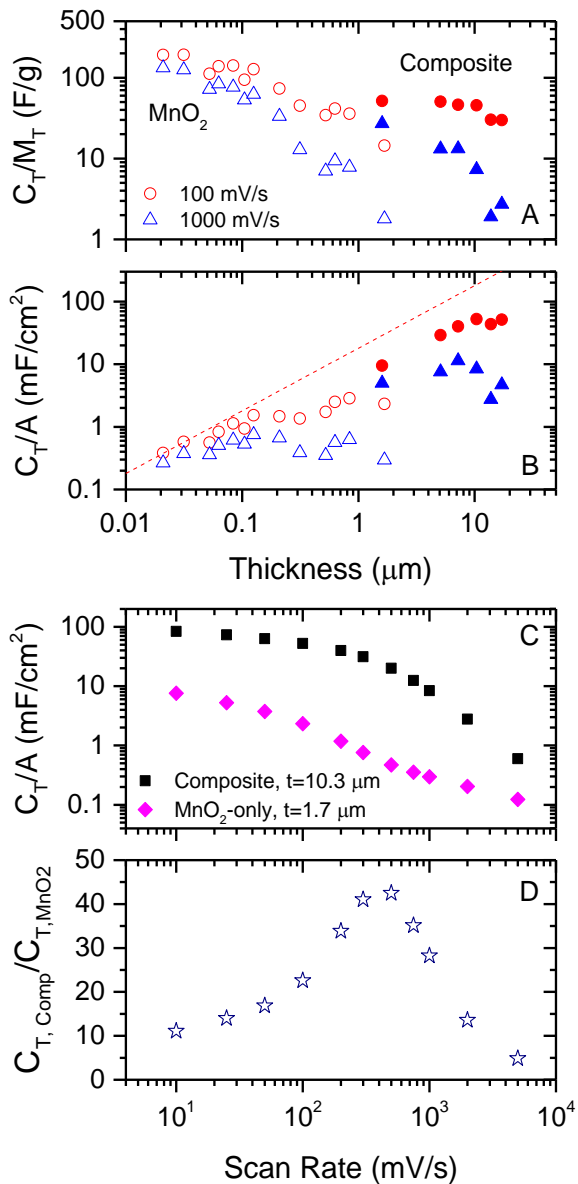


Figure 6: A) Specific capacitance and B) areal capacitance as a function of electrode thickness. This data is shown for electrodes produced from both MnO<sub>2</sub>-only (open symbols) and MnO<sub>2</sub>-SWNT composite (15 vol %, closed symbols) films, measured at two different scan rates. C) Areal capacitance plotted *versus* scan rate for the thickest MnO<sub>2</sub>-only electrode we were able to produce and a 15 vol% SWNT-MnO<sub>2</sub> composite electrode with optimised thickness. D) Ratio of the capacitance of composite and MnO<sub>2</sub>-only electrodes shown in C plotted *versus* scan rate. This data shows the increase in capacitance achievable by adding nanotubes due to the combination of percolative effects and the ability to make thicker electrodes in the presence of nanotubes.

## References

1. Geim, A. K., Graphene: Status and Prospects. *Science* **2009**, *324*, 1530-1534.
2. Chhowalla, M.; Shin, H. S.; Eda, G.; Li, L.-J.; Loh, K. P.; Zhang, H., The Chemistry of Two-Dimensional Layered Transition Metal Dichalcogenide Nanosheets. *Nat. Chem.* **2013**, *5*, 263-275.
3. Wang, Q. H.; Kalantar-Zadeh, K.; Kis, A.; Coleman, J. N.; Strano, M. S., Electronics and Optoelectronics of Two-Dimensional Transition Metal Dichalcogenides. *Nat. Nanotechnol.* **2012**, *7*, 699-712.
4. Osada, M.; Sasaki, T., Two-Dimensional Dielectric Nanosheets: Novel Nanoelectronics from Nanocrystal Building Blocks. *Adv. Mater.* **2012**, *24*, 210-228.
5. Liu, H.; Neal, A. T.; Zhu, Z.; Luo, Z.; Xu, X.; Tománek, D.; Ye, P. D., Phosphorene: An Unexplored 2d Semiconductor with a High Hole Mobility. *ACS Nano* **2014**, *8*, 4033-4041.
6. Coleman, J. N.; Lotya, M.; O'Neill, A.; Bergin, S. D.; King, P. J.; Khan, U.; Young, K.; Gaucher, A.; De, S.; Smith, R. J., *et al.*, Two-Dimensional Nanosheets Produced by Liquid Exfoliation of Layered Materials. *Science* **2011**, *331*, 568-571.
7. Nicolosi, V.; Chhowalla, M.; Kanatzidis, M. G.; Strano, M. S.; Coleman, J. N., Liquid Exfoliation of Layered Materials. *Science* **2013**, *340*, 1420.
8. Zeng, Z. Y.; Yin, Z. Y.; Huang, X.; Li, H.; He, Q. Y.; Lu, G.; Boey, F.; Zhang, H., Single-Layer Semiconducting Nanosheets: High-Yield Preparation and Device Fabrication. *Angew. Chem.-Int. Edit.* **2011**, *50*, 11093-11097.
9. Eda, G.; Yamaguchi, H.; Voiry, D.; Fujita, T.; Chen, M.; Chhowalla, M., Photoluminescence from Chemically Exfoliated Mos<sub>2</sub>. *Nano Lett.* **2011**, *11*, 5111-5116.
10. Lukatskaya, M. R.; Mashtalir, O.; Ren, C. E.; Dall'Agnesse, Y.; Rozier, P.; Taberna, P. L.; Naguib, M.; Simon, P.; Barsoum, M. W.; Gogotsi, Y., Cation Intercalation and High Volumetric Capacitance of Two-Dimensional Titanium Carbide. *Science* **2013**, *341*, 1502-1505.
11. Liu, J.; Liu, X.-W., Two-Dimensional Nanoarchitectures for Lithium Storage. *Adv. Mater.* **2012**, *24*, 4097-4111.
12. Backes, C.; Smith, R. J.; McEvoy, N.; Berner, N. C.; McCloskey, D.; Nerl, H. C.; O'Neill, A.; King, P. J.; Higgins, T.; Hanlon, D., *et al.*, Edge and Confinement Effects Allow *in Situ* Measurement of Size and Thickness of Liquid-Exfoliated Nanosheets. *Nat. Commun.* **2014**, *5*, 4576.
13. Voiry, D.; Yamaguchi, H.; Li, J.; Silva, R.; Alves, D. C. B.; Fujita, T.; Chen, M.; Asefa, T.; Shenoy, V. B.; Eda, G., *et al.*, Enhanced Catalytic Activity in Strained Chemically Exfoliated Ws<sub>2</sub> Nanosheets for Hydrogen Evolution. *Nat. Mater.* **2013**, *12*, 850-855.
14. Wang, J.-Z.; Lu, L.; Lotya, M.; Coleman, J. N.; Chou, S.-L.; Liu, H.-K.; Minett, A. I.; Chen, J., Development of Mos<sub>2</sub>-Cnt Composite Thin Film from Layered Mos<sub>2</sub> for Lithium Batteries. *Adv. Energy Mater.* **2013**, *3*, 798-805.
15. Chang, K.; Chen, W., L-Cysteine-Assisted Synthesis of Layered Mos<sub>2</sub>/Graphene Composites with Excellent Electrochemical Performances for Lithium Ion Batteries. *ACS Nano* **2011**, *5*, 4720-4728.
16. Tai, S.-Y.; Liu, C.-J.; Chou, S.-W.; Chien, F. S.-S.; Lin, J.-Y.; Lin, T.-W., Few-Layer Mos<sub>2</sub> Nanosheets Coated onto Multi-Walled Carbon Nanotubes as a Low-Cost and Highly Electrocatalytic Counter Electrode for Dye-Sensitized Solar Cells. *J. Mater. Chem.* **2012**, *22*, 24753-24759.
17. Suzuki, S.; Miyayama, M., Lithium Intercalation Properties of Octatitanate Synthesized through Exfoliation/Reassembly. *J. Phys. Chem. B* **2006**, *110*, 4731-4734.
18. Wang, L. Z.; Takada, K.; Kajiyama, A.; Onoda, M.; Michiue, Y.; Zhang, L. Q.; Watanabe, M.; Sasaki, T., Synthesis of a Li-Mn-Oxide with Disordered Layer Stacking through Flocculation of Exfoliated Mno<sub>2</sub> Nanosheets, and Its Electrochemical Properties. *Chem. Mater.* **2003**, *15*, 4508-4514.
19. Lee, C. Y.; Tsai, H. M.; Chuang, H. J.; Li, S. Y.; Lin, P.; Tseng, T. Y., Characteristics and Electrochemical Performance of Supercapacitors with Manganese Oxide-Carbon Nanotube Nanocomposite Electrodes. *J. Electrochem. Soc.* **2005**, *152*, A716-A720.
20. Park, H.-Y.; Shin, T. J.; Joh, H.-I.; Jang, J. H.; Ahn, D.; Yoo, S. J., Graphene-Oxide-Intercalated Layered Manganese Oxides as an Efficient Oxygen Reduction Reaction Catalyst in Alkaline Media. *Electrochem. Commun.* **2014**, *41*, 35-38.

21. Son, J. S.; Choi, M. K.; Han, M. K.; Park, K.; Kim, J. Y.; Lim, S. J.; Oh, M.; Kuk, Y.; Park, C.; Kim, S. J., *et al.*, N-Type Nanostructured Thermoelectric Materials Prepared from Chemically Synthesized Ultrathin Bi<sub>2</sub>Te<sub>3</sub> Nanoplates. *Nano Lett.* **2012**, *12*, 640-647.
22. Conway, B. E., *Electrochemical Supercapacitors: Scientific Fundamentals and Technological Applications*. 1 ed.; Springer: 1999.
23. Sugimoto, W.; Iwata, H.; Yasunaga, Y.; Murakami, Y.; Takasu, Y., Preparation of Ruthenic Acid Nanosheets and Utilization of Its Interlayer Surface for Electrochemical Energy Storage. *Angew. Chem.-Int. Edit.* **2003**, *42*, 4092-4096.
24. Brezesinski, T.; Wang, J.; Tolbert, S. H.; Dunn, B., Ordered Mesoporous [Alpha]-Moo<sub>3</sub> with Iso-Oriented Nanocrystalline Walls for Thin-Film Pseudocapacitors. *Nat. Mater.* **2010**, *9*, 146-151.
25. Toupin, M.; Brousse, T.; Belanger, D., Charge Storage Mechanism of Mno<sub>2</sub> Electrode Used in Aqueous Electrochemical Capacitor. *Chem. Mater.* **2004**, *16*, 3184-3190.
26. Yu, W.; Jiang, X.; Ding, S.; Li, B. Q., Preparation and Electrochemical Characteristics of Porous Hollow Spheres of Nio Nanosheets as Electrodes of Supercapacitors. *J. Power Sources* **2014**, *256*, 440-448.
27. Wang, G.; Huang, J.; Chen, S.; Gao, Y.; Cao, D., Preparation and Supercapacitance of Cuo Nanosheet Arrays Grown on Nickel Foam. *J. Power Sources* **2011**, *196*, 5756-5760.
28. Sugimoto, W.; Yokoshima, K.; Ohuchi, K.; Murakami, Y.; Takasu, Y., Fabrication of Thin-Film, Flexible, and Transparent Electrodes Composed of Ruthenic Acid Nanosheets by Electrophoretic Deposition and Application to Electrochemical Capacitors. *J. Electrochem. Soc.* **2006**, *153*, A255-A260.
29. Rakhi, R. B.; Chen, W.; Hedhili, M. N.; Cha, D.; Alshareef, H. N., Enhanced Rate Performance of Mesoporous Co<sub>3</sub>O<sub>4</sub> Nanosheet Supercapacitor Electrodes by Hydrous RuO<sub>2</sub> Nanoparticle Decoration. *ACS Appl. Mater. Interfaces* **2014**, *6*, 4196-4206.
30. Hanlon, D.; Backes, C.; Higgins, T. M.; Hughes, M.; O'Neill, A.; King, P. J.; McEvoy, N.; Duesberg, G. S.; Mendoza Sanchez, B.; Pettersson, H., *et al.*, Production of Molybdenum Trioxide Nanosheets by Liquid Exfoliation and Their Application in High-Performance Supercapacitors. *Chem. Mater.* **2014**, *26*, 1751-1763.
31. Sun, X.; Wang, G.; Hwang, J.-Y.; Lian, J., Porous Nickel Oxide Nano-Sheets for High Performance Pseudocapacitance Materials. *J. Mater. Chem.* **2011**, *21*, 16581.
32. Song, M.-S.; Lee, K. M.; Lee, Y. R.; Kim, I. Y.; Kim, T. W.; Gunjekar, J. L.; Hwang, S.-J., Porously Assembled 2d Nanosheets of Alkali Metal Manganese Oxides with Highly Reversible Pseudocapacitance Behaviors. *J. Phys. Chem. C* **2010**, *114*, 22134-22140.
33. Wang, L.; Lin, C.; Zhang, F.; Jin, J., Phase Transformation Guided Single-Layer B-Co(OH)<sub>2</sub> Nanosheets for Pseudocapacitive Electrodes. *ACS Nano* **2014**, *8*, 3724-3734.
34. Zhu, J.; Cao, L.; Wu, Y.; Gong, Y.; Liu, Z.; Hoster, H. E.; Zhang, Y.; Zhang, S.; Yang, S.; Yan, Q., *et al.*, Building 3d Structures of Vanadium Pentoxide Nanosheets and Application as Electrodes in Supercapacitors. *Nano Lett.* **2013**, *13*, 5408-5413.
35. Ma, R.; Liu, X.; Liang, J.; Bando, Y.; Sasaki, T., Molecular-Scale Heteroassembly of Redoxable Hydroxide Nanosheets and Conductive Graphene into Superlattice Composites for High-Performance Supercapacitors. *Adv. Mater.* **2014**, *26*, 4173-4178.
36. Paton, K. R.; Varrla, E.; Backes, C.; Smith, R. J.; Khan, U.; O'Neill, A.; Boland, C.; Lotya, M.; Istrate, O. M.; King, P. J., *et al.*, Scalable Production of Large Quantities of Defect-Free Few-Layer Graphene by Shear Exfoliation in Liquids. *Nat. Mater.* **2014**, *13*, 624-630.
37. Pang, S.-C.; Anderson, M. A.; Chapman, T. W., Novel Electrode Materials for Thin-Film Ultracapacitors: Comparison of Electrochemical Properties of Sol-Gel-Derived and Electrodeposited Manganese Dioxide. *J. Electrochem. Soc.* **2000**, *147*, 444-450.
38. Broughton, J. N.; Brett, M. J., Investigation of Thin Sputtered Mn Films for Electrochemical Capacitors. *Electrochimica Acta* **2004**, *49*, 4439-4446.
39. Lee, H. Y.; Kim, S. W.; Lee, H. Y., Expansion of Active Site Area and Improvement of Kinetic Reversibility in Electrochemical Pseudocapacitor Electrode. *Electrochem. Solid-State Lett.* **2001**, *4*, A19-A22.
40. Belanger, D.; Brousse, T.; Long, J. W., Manganese Oxides: Battery Materials Make the Leap to Electrochemical Capacitors. *Electrochem. Soc. Interface* **2008**, *17*, 49-52.

41. Xu, C.; Kang, F.; Li, B.; Du, H., Recent Progress on Manganese Dioxide Based Supercapacitors. *J. Mater. Res.* **2010**, *25*, 1421-1432.
42. Raymundo-Pinero, E.; Khomenko, V.; Frackowiak, E.; Beguin, F., Performance of Manganese Oxide/Cnts Composites as Electrode Materials for Electrochemical Capacitors. *J. Electrochem. Soc.* **2005**, *152*, A229-A235.
43. Yu, G.; Hu, L.; Liu, N.; Wang, H.; Vosgueritchian, M.; Yang, Y.; Cui, Y.; Bao, Z., Enhancing the Supercapacitor Performance of Graphene/Mno<sub>2</sub> Nanostructured Electrodes by Conductive Wrapping. *Nano Lett.* **2011**, *11*, 4438.
44. Lee, H. Y.; Goodenough, J. B., Supercapacitor Behavior with KCl Electrolyte. *J. Solid State Chem.* **1999**, *144*, 220-223.
45. Jiang, H.; Sun, T.; Li, C.; Ma, J., Hierarchical Porous Nanostructures Assembled from Ultrathin Mno<sub>2</sub> Nanoflakes with Enhanced Supercapacitive Performances. *J. Mater. Chem.* **2011**, *22*, 2751-2756.
46. Zhi, M.; Xiang, C.; Li, J.; Li, M.; Wu, N., Nanostructured Carbon–Metal Oxide Composite Electrodes for Supercapacitors: A Review. *Nanoscale* **2012**, *5*, 72-88.
47. Cunningham, G.; Lotya, M.; McEvoy, N.; Duesberg, G. S.; van der Schoot, P.; Coleman, J. N., Percolation Scaling in Composites of Exfoliated Mos<sub>2</sub> Filled with Nanotubes and Graphene. *Nanoscale* **2012**, *4*, 6260-6264.
48. Kim, H.; Popov, B. N., Synthesis and Characterization of Mno<sub>2</sub>-Based Mixed Oxides as Supercapacitors. *J. Electrochem. Soc.* **2003**, *150*, D56-D62.
49. Zhou, Y. K.; He, B. L.; Zhang, F. B.; Li, H. L., Hydrous Manganese Oxide/Carbon Nanotube Composite Electrodes for Electrochemical Capacitors. *J. Solid State Electrochem* **2004**, *8*, 482-487.
50. Hu, C.-C.; Tsou, T.-W., Capacitive and Textural Characteristics of Hydrous Manganese Oxide Prepared by Anodic Deposition. *Electrochimica Acta* **2002**, *47*, 3523-3532.
51. Wei, W.; Cui, X.; Chen, W.; Ivey, D. G., Phase-Controlled Synthesis of Mno<sub>2</sub> Nanocrystals by Anodic Electrodeposition: Implications for High-Rate Capability Electrochemical Supercapacitors. *J. Phys. Chem. C* **2008**, *112*, 15075-15083.
52. Coelho, J.; Mendoza-Sanchez, B.; Pettersson, H.; Pokle, A.; McGuire, E. K.; Long, E.; McKeon, L.; Bell, A. P.; Nicolosi, V., Manganese Oxide Nanosheets and a 2d Hybrid of Graphene-Manganese Oxide Nanosheets Synthesized by Liquid-Phase Exfoliation. *arXiv:1409.1087 [cond-mat.mtrl-sci]* **2014**.
53. Julien, C.; Massot, M.; Baddour-Hadjean, R.; Franger, S.; Bach, S.; Pereira-Ramos, J. P., Raman Spectra of Birnessite Manganese Dioxides. *Solid State Ionics* **2003**, *159*, 345-356.
54. Hsu, Y.-K.; Chen, Y.-C.; Lin, Y.-G.; Chen, L.-C.; Chen, K.-H., Birnessite-Type Manganese Oxides Nanosheets with Hole Acceptor Assisted Photoelectrochemical Activity in Response to Visible Light. *J. Mater. Chem.* **2012**, *22*, 2733-2739.
55. Hsu, Y.-K.; Chen, Y.-C.; Lin, Y.-G.; Chen, L.-C.; Chen, K.-H., Reversible Phase Transformation of Mno<sub>2</sub> Nanosheets in an Electrochemical Capacitor Investigated by *in Situ* Raman Spectroscopy. *Chem. Commun.* **2011**, *47*, 1252-1254.
56. Ogata, A.; Komaba, S.; Baddour-Hadjean, R.; Pereira-Ramos, J. P.; Kumagai, N., Doping Effects on Structure and Electrode Performance of K-Birnessite-Type Manganese Dioxides for Rechargeable Lithium Battery. *Electrochimica Acta* **2008**, *53*, 3084-3093.
57. Biesinger, M. C.; Payne, B. P.; Grosvenor, A. P.; Lau, L. W. M.; Gerson, A. R.; Smart, R. S., Resolving Surface Chemical States in Xps Analysis of First Row Transition Metals, Oxides and Hydroxides: Cr, Mn, Fe, Co and Ni. *Appl. Surf. Sci.* **2011**, *257*, 2717-2730.
58. Hu, C.-C.; Tsou, T.-W., Ideal Capacitive Behavior of Hydrous Manganese Oxide Prepared by Anodic Deposition. *Electrochem. Commun.* **2002**, *4*, 105-109.
59. Wu, Z. C.; Chen, Z. H.; Du, X.; Logan, J. M.; Sippel, J.; Nikolou, M.; Kamaras, K.; Reynolds, J. R.; Tanner, D. B.; Hebard, A. F., *et al.*, Transparent, Conductive Carbon Nanotube Films. *Science* **2004**, *305*, 1273-1276.
60. Miller, J. R., Introduction to Electrochemical Capacitor Technology. *Electrical Insulation Magazine, IEEE* **2010**, *26*, 40-47.
61. Zhu, G.; Li, H.; Deng, L.; Liu, Z.-H., Low-Temperature Synthesis of  $\Delta$ -Mno<sub>2</sub> with Large Surface Area and Its Capacitance. *Materials Letters* **2010**, *64*, 1763-1765.

62. Stoller, M. D.; Ruoff, R. S., Best Practice Methods for Determining an Electrode Material's Performance for Ultracapacitors. *Energy Environ. Sci.* **2010**, *3*, 1294.
63. Wu, Y.-T.; Hu, C.-C., Effects of Electrochemical Activation and Multiwall Carbon Nanotubes on the Capacitive Characteristics of Thick MnO<sub>2</sub> Deposits. *J. Electrochem. Soc.* **2004**, *151*, A2060-A2066.
64. Chen, Y.-S.; Hu, C.-C.; Wu, Y.-T., Capacitive and Textural Characteristics of Manganese Oxide Prepared by Anodic Deposition: Effects of Manganese Precursors and Oxide Thickness. *Journal of Solid State Electrochemistry* **2004**, *8*, 467-473.
65. Broughton, J. N.; Brett, M. J., Variations in MnO<sub>2</sub> Electrodeposition for Electrochemical Capacitors. *Electrochimica Acta* **2005**, *50*, 4814-4819.
66. Nam, K.-W.; Kim, K.-B., Manganese Oxide Film Electrodes Prepared by Electrostatic Spray Deposition for Electrochemical Capacitors. *J. Electrochem. Soc.* **2006**, *153*, A81-A88.
67. Nagarajan, N.; Cheong, M.; Zhitomirsky, I., Electrochemical Capacitance of MnO<sub>x</sub> Films. *Materials Chemistry and Physics* **2007**, *103*, 47-53.
68. Wimalasiri, Y.; Fan, R.; Zhao, X. S.; Zou, L., Assembly of Ni-Al Layered Double Hydroxide and Graphene Electrodes for Supercapacitors. *Electrochimica Acta* **2014**, *134*, 127-135.
69. Doherty, E. M.; De, S.; Lyons, P. E.; Shmeliov, A.; Nirmalraj, P. N.; Scardaci, V.; Joimel, J.; Blau, W. J.; Boland, J. J.; Coleman, J. N., The Spatial Uniformity and Electromechanical Stability of Transparent, Conductive Films of Single Walled Nanotubes. *Carbon* **2009**, *47*, 2466-2473.
70. Subramanian, V.; Zhu, H.; Wei, B., Synthesis and Electrochemical Characterizations of Amorphous Manganese Oxide and Single Walled Carbon Nanotube Composites as Supercapacitor Electrode Materials. *Electrochem. Commun.* **2006**, *8*, 827-832.
71. Lu, X.; Dou, H.; Gao, B.; Yuan, C.; Yang, S.; Hao, L.; Shen, L.; Zhang, X., A Flexible Graphene/Multiwalled Carbon Nanotube Film as a High Performance Electrode Material for Supercapacitors. *Electrochimica Acta* **2011**, *56*, 5115-5121.
72. Toupin, M.; Brousse, T.; Belanger, D., Influence of Microstructure on the Charge Storage Properties of Chemically Synthesized Manganese Dioxide. *Chem. Mater.* **2002**, *14*, 3946-3952.
73. Lee, S. W.; Kim, J.; Chen, S.; Hammond, P. T.; Shao-Horn, Y., Carbon Nanotube/Manganese Oxide Ultrathin Film Electrodes for Electrochemical Capacitors. *ACS Nano* **2010**, *4*, 3889-3896.
74. Khan, U.; O'Connor, I.; Gun'ko, Y. K.; Coleman, J. N., The Preparation of Hybrid Films of Carbon Nanotubes and Nano-Graphite/Graphene with Excellent Mechanical and Electrical Properties. *Carbon* **2010**, *48*, 2825-2830.
75. Brousse, T.; Toupin, M.; Belanger, D., A Hybrid Activated Carbon-Manganese Dioxide Capacitor Using a Mild Aqueous Electrolyte. *J. Electrochem. Soc.* **2004**, *151*, A614-A622.
76. Stauffer, D. S.; Aharony, A., *Introduction to Percolation Theory*. Taylor and Francis: London, 1994.
77. Bauhofer, W.; Kovacs, J. Z., A Review and Analysis of Electrical Percolation in Carbon Nanotube Polymer Composites. *Compos. Sci. Technol.* **2009**, *69*, 1486-1498.
78. Foygel, M.; Morris, R. D.; Anez, D.; French, S.; Sobolev, V. L., Theoretical and Computational Studies of Carbon Nanotube Composites and Suspensions: Electrical and Thermal Conductivity. *Phys. Rev. B* **2005**, *71*, 104201.
79. King, P. J.; Higgins, T. M.; De, S.; Nicoloso, N.; Coleman, J. N., Percolation Effects in Supercapacitors with Thin, Transparent Carbon Nanotube Electrodes. *ACS Nano* **2012**, *4*, 7064-7072.
80. Wu, N. L.; Wang, S. Y., Conductivity Percolation in Carbon-Carbon Supercapacitor Electrodes. *J. Power Sources* **2002**, *110*, 233-236.
81. Lv, G.; Wu, D.; Fu, R.; Zhang, Z.; Su, Z., Electrochemical Properties of Conductive Filler/Carbon Aerogel Composites as Electrodes of Supercapacitors. *Journal of Non-Crystalline Solids* **2008**, *354*, 4567-4571.
82. Yang, X.-h.; Wang, Y.-g.; Xiong, H.-m.; Xia, Y.-y., Interfacial Synthesis of Porous MnO<sub>2</sub> and Its Application in Electrochemical Capacitor. *Electrochimica Acta* **2007**, *53*, 752-757.
83. Yuan, A.; Wang, X.; Wang, Y.; Hu, J., Textural and Capacitive Characteristics of MnO<sub>2</sub> Nanocrystals Derived from a Novel Slide-Reaction Route. *Electrochimica Acta* **2009**, *54*, 1021-1026.
84. Reddy, R. N.; Reddy, R. G., Sol-Gel MnO<sub>2</sub> as an Electrode Material for Electrochemical Capacitors. *J. Power Sources* **2003**, *124*, 330-337.

85. Wang, G.-X.; Zhang, B.-L.; Yu, Z.-L.; Qu, M.-Z., Manganese Oxide/Mwnts Composite Electrodes for Supercapacitors. *Solid State Ionics* **2005**, *176*, 1169-1174.
86. White, S. I.; DiDonna, B. A.; Mu, M.; Lubensky, T. C.; Winey, K. I., Simulations and Electrical Conductivity of Percolated Networks of Finite Rods with Various Degrees of Axial Alignment. *Phys. Rev. B* **2009**, *79*, 024301.
87. Scardaci, V.; Coull, R.; Lyons, P. E.; Rickard, D.; Coleman, J. N., Spray Deposition of Highly Transparent, Low-Resistance Networks of Silver Nanowires over Large Areas. *Small* **2011**, *7*, 2621-2628.
88. Balberg, I., Tunnelling and Nonuniversal Conductivity in Composite-Materials. *Phys. Rev. Lett.* **1987**, *59*, 1305-1308.
89. Pico, F.; Pecharroman, C.; Ansón, A.; Martínez, M. T.; Rojo, J. M., Understanding Carbon–Carbon Composites as Electrodes of Supercapacitors a Study by Ac and Dc Measurements. *J. Electrochem. Soc.* **2007**, *154*, A579-A586.
90. Okamura, K.; Inoue, R.; Seville, T.; Tomono, K.; Nakayama, M., An Approach to Optimize the Composition of Supercapacitor Electrodes Consisting of Manganese-Molybdenum Mixed Oxide and Carbon Nanotubes. *J. Electrochem. Soc.* **2011**, *158*, A711.
91. Wen, S.; Lee, J.-W.; Yeo, I.-H.; Park, J.; Mho, S.-i., The Role of Cations of the Electrolyte for the Pseudocapacitive Behavior of Metal Oxide Electrodes, Mno<sub>2</sub> and RuO<sub>2</sub>. *Electrochimica Acta* **2004**, *50*, 849-855.